

Readout electronics of a prototype time-of-flight ion composition analyzer for space plasma

Di Yang^{1,2} · Zhe Cao^{1,2} · Xin-Jun Hao^{3,4} · Yi-Ren Li^{3,4} · Shu-Bin Liu^{1,2} · Chang-Qing Feng^{1,2} · Qi An^{1,2}

Received: 13 February 2017/Revised: 13 April 2017/Accepted: 19 April 2017/Published online: 21 March 2018
© Shanghai Institute of Applied Physics, Chinese Academy of Sciences, Chinese Nuclear Society, Science Press China and Springer Nature Singapore Pte Ltd. 2018

Abstract Readout electronics is developed for a prototype time-of-flight (TOF) ion composition spectrometer for in situ measurement of the mass/charge distributions of major ion species from 200 to 100 keV/e in space plasma. By utilizing a constant fraction discriminator (CFD) and time-to-digital converter (TDC), challenging dynamic range measurements were performed with high time resolution and event rates. CFD was employed to discriminate the TOF signals from the micro-channel plate and channel electron multipliers. TDC based on the combination of counter and OR-gate delay chain was designed in a high-reliability flash field programmable gate array. Owing to the non-uniformity of the delay chain, a correction algorithm based on integral nonlinearity compensation was implemented to reduce the time uncertainty. The test results showed that the electronics achieved a low timing

error of < 200 ps in the input range from 35 to 500 mV for the CFD, and a time resolution of ~ 550 ps with time uncertainty < 180 ps after correction and a time range of $6.4 \mu\text{s}$ for the TDC. The TOF spectrum from an electron beam experiment of the impacting N_2 gas further indicated the good performance of this readout electronic.

Keywords Space plasma · Ion composition analyzer · Readout electronics · Constant fraction discriminator · Time-to-digital converter

1 Introduction

The realization of ion composition measurements has made significant contributions to space plasma experiments over the past few decades. For example, He^+ pickup ions in the solar wind present an important source for ion reflection and heating [1]; CO^{2+} and O^{2+} measurements provide the details of a further process of the escape mechanism for the Martian upper atmosphere and ionosphere [2, 3]. Among the different instruments, the time-of-flight (TOF) mass-spectrograph has become a standard tool in space plasma physics because of the excellent capabilities of measuring both the particle energy and speed. This allows for the determination of the particle mass of atomic species in the energy range of the bulk plasma, as well as in the energy gap between ~ 30 and several hundred kiloelectronvolts [4], with extensive applicability to different space missions such as the PLASTIC spectrometer for the STEREO mission [5] and the STATIC instrument for the MAVEN mission [6].

A TOF ion composition analyzer is being developed to provide in situ measurements of the population

This work was supported by the National Key Scientific Instrument and Equipment Development Projects of the National Natural Science Foundation of China (No. 41327802) and China Mars Project.

✉ Zhe Cao
caozhe@ustc.edu.cn

Qi An
anqi@ustc.edu.cn

¹ State Key Laboratory of Particle Detection and Electronics, University of Science and Technology of China, Hefei 230026, China

² Department of Modern Physics, University of Science and Technology of China, Hefei 230026, China

³ Division of Space Physics, University of Science and Technology of China, Hefei 230026, China

⁴ CAS Key Laboratory of Geospace Environment, Hefei 230026, China

distributions of the major ion species (e.g., C, O, Mg, Si, and Fe) in interplanetary space to study the solar wind origins and acceleration. It consists of an entrance deflection subsystem, a post-acceleration subsystem, a TOF chamber, and an electronics box. A simplified cross section and block diagram of this sensor is given in Fig. 1. The entrance deflection subsystem, comprised of a main and small sector as well as a cylindrically symmetric electrostatic analyzer (ESA), collects the incident ions through two channels activated and sequentially switched by the electronics. The small and main channels gather the major solar wind ions (H and He) ranging from 0.2 to 10 keV/e and different ion species covering 0.2–100 keV/e, respectively. The ESA with an intrinsic energy resolution of $\Delta E/E < 15\%$, controlled by a sweeping high voltage (HV) between its inner and outer hemisphere, filters the collected ions according to their energy per charge (E/Q). The post-acceleration subsystem accelerates ions via a potential drop of up to 10 kV to ensure that the ions pass through the foil with relatively little energy straggling and angular scattering just before entering the TOF chamber. The TOF subsystem is a combination of a grid-supported carbon foil, a 20-cm region of linearly increasing electric field (LEF),

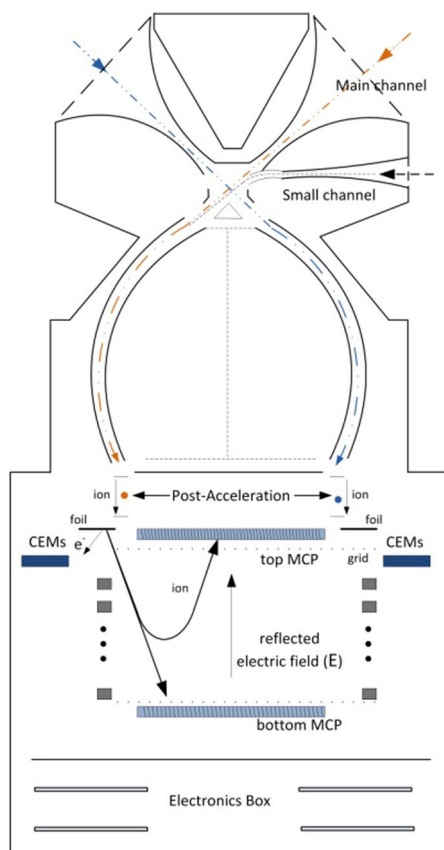


Fig. 1 (Color online) Simplified structural diagram of the TOF spectrometer

16 channel electron multipliers (CEMs), two micro-channel plates (MCPs) in chevron pair configuration, and 18 discrete anodes. Secondary electrons are emitted from the carbon foil during the passage of the ions and accelerated and deflected onto a CEM by an appropriate potential configuration, providing a fast start timing signal (with a typical leading edge of ~ 1 ns) and azimuth information for the angular sectoring. The original incident particle continues through the TOF chamber, striking either a top MCP assembly with initial energies of < 15 keV/q or a bottom MCP with energies greater than the turn-around energy (15 keV/q), yielding a fast stop timing signal.

Owing to the 0.2–100 keV/e large energy range covering the slow solar wind and superthermal ions, the spectrometer must be sensitive to differential energy fluxes up to 10^{12} eV/[cm² s sr eV] [5, 7], and the readout electronics require the capability of counting at megahertz (MHz) rates. To perform the measurements of different ion species, from H to Fe, a sufficient time resolution with low dispersal [$< 0.6 \pm 0.2$ (ns)] as well as a background noise suppression measure [8] is required by the TOF system in the design of the readout electronics. Furthermore, the largest flying time of the ion species simulated by the SIMION software can reach up to a few microseconds (< 5 μ s), providing a new challenge for the dynamic range of time measurements compared with other similar instruments. Different instrumentations have been applied for ion composition measurements [2, 5, 6], and a readout system with such a high event rate, high time resolution, and large time range is not usually applied to space applications. In this paper, we focus on the design of the readout electronics for a space mission to provide the TOF measurement and the performance test.

2 Electronics implementation

Based on the principle of reflecting ions in a linearly increasing electric field (LEF), the mass per charge (M/Q) of the ions is determined by Eq. (1) [9]:

$$M/Q = 2(E/Q + e \cdot U_{ACC}) / (d/\tau)^2 \cdot \alpha, \quad (1)$$

where M , Q , and E are the ion's mass, charge, and kinetic energy, respectively; U_{ACC} is the post-acceleration voltage; d is the length of the TOF region; τ is the flight time of the ions; and α represents the effect of energy loss in the thin carbon foil (≈ 3 μ g/cm²). According to the equation, the ion species population can be resolved by M/Q , which is closely associated with the time of flight, and the E/Q determined by the ESA. Therefore, it is crucial that the flight time is measured accurately, expressed as the time interval of the start and stop signals, so as to meet the experiment requirement.

Different readout methods are used for the time measurement for many space programs. Those readout electronics mostly contain time-to-digit converter (TDC) and timing circuitry that are usually achieved by the constant fraction discriminator (CFD) rather than the leading-edge discriminator (LED) for high-accuracy applications. The TDC can be mainly implemented by three approaches: (1) the traditional combination of time-to-amplitude and analog-to-digital converter (TAC + ADC) observed in PLASTIC and STATIC on the Cluster and MAVEN missions, respectively [5, 6]; (2) the TDC-ASIC, such as TDC-GP1/GP2 chips, applied by the LTT experiment on the COMPASS project [10]; and (3) TDC implementation on radiation-hardened field programmable gate array (FPGA) [11–13]. Although TAC + ADC techniques can provide a high time resolution, these have large dead time (typically > 1 μs) as well as large power dissipation because of the high-speed sampling, which does not satisfy our requirement. Compared with the TAC + ADC technique, TDC-ASIC has an extremely high integration and fine resolution, but its limited time interval measurement range or large dead time was not suitable for our experiment [14]. The combination of time interpolating and the counter in FPGA provides a good resolution and programmable dynamic range adjusted by counters; the inherent pipelining processing of FPGA brings out a very small dead time (< 125 ns), meeting the demand of a high event rate. Owing to the rapid development of integrated circuits, system-on-chip (SOC) chips including CFDs and TDC circuitry have emerged with successful applications, for example, the ESP instrument on the Messenger mission [15]. Although these have advantages of high integration and low power consumption over the implementation of TDC in FPGA, there are constraints on the measurement range, similar to some TDC-ASIC chips. Based on the above discussion, a readout scheme based on CFD timing and TDC of time interpolation, implemented in a high-reliability FPGA together with an RS422 interface to communicate with the housekeeping computer on the

satellite (S/C), was adopted for the TOF ion composition spectrometer.

As shown in Fig. 2, the top-level diagram of the TOF readout electronics was mainly composed of the CFD unit, FPGA-TDC unit, status monitoring unit, and control and data processing unit (CDPU).

2.1 CFD unit

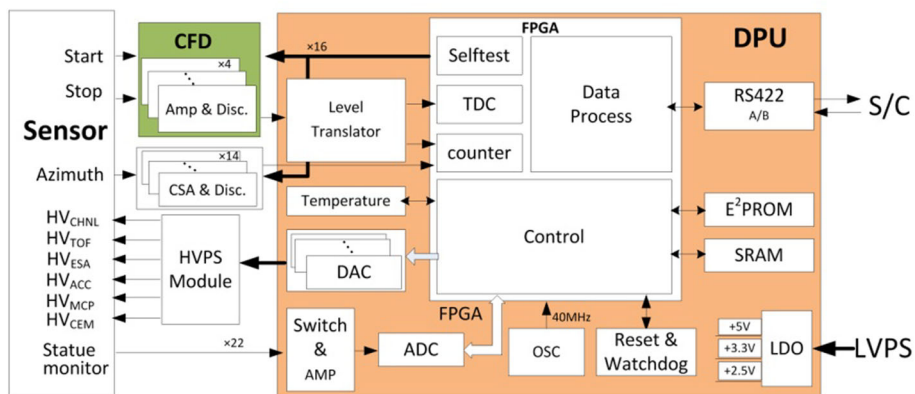
To eliminate the time walk effect caused by both the amplitude and edge variation of the sensor signal, four CFD circuits were designed to process the start and stop signals, mainly comprised of an amplifier, two comparators, two D-flip-flops (DFFs), and an AND-gate, as shown in Fig. 3. In view of the fast leading-edge signals generated by both the MCPs and CEMs, a fast current-feedback amplifier with enough bandwidth (AD8001, from ADI Corp.) for every channel was employed to magnify its feeding negative pulse after capacitive coupling, without seriously slowing the signal edge containing the timing information. Then the amplified signal output from AD8001 was split into three parts, with one part fed to the negative end of a high-speed comparator (MAX9202) after a fixed delay and a second part delivered to the positive end with an amplitude attenuation achieved by a resistance divider. The relationship between the attenuation ratio and delay length can be described by Eq. (2):

$$t_d < (1 - f) \times t_r, \tag{2}$$

where t_d is the delay length of the delay line, f is the amplitude attenuation ratio, and t_r is the forward-edge pulse time.

To remove miss-firing caused by noise or interruption to the CFD discriminator, a coincidence circuit containing a comparator, DFF, and an AND-gate was added. Both the third part from AD8001 and a threshold voltage controlled by a digital-to-analog converter (DAC) shared by all CFDs were sent to the negative and positive ends of the comparator, respectively. If the signal exceeded the threshold

Fig. 2 (Color online) Top-level diagram of the readout electronics



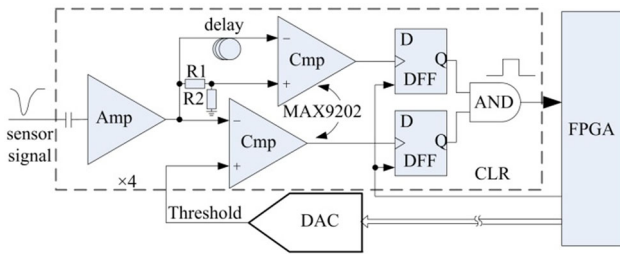


Fig. 3 Schematic of the CFD circuitry

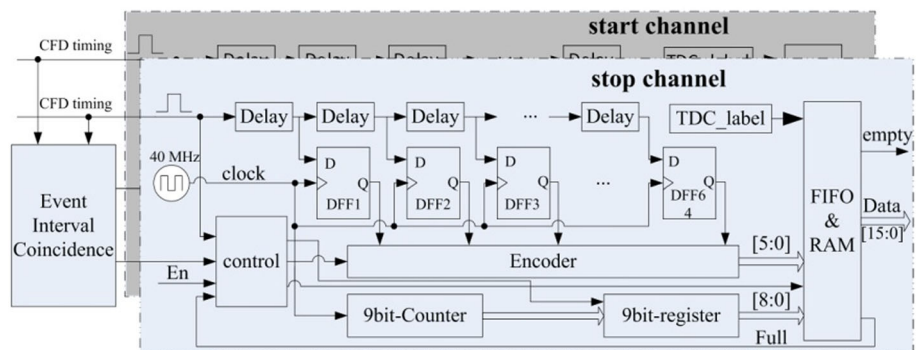
voltage applied to the comparator, the output was true until the signal dropped below the threshold. After tracking the rising edge, both the DFFs were fed to an AND-gate to produce an event coincidence.

2.2 FPGA-TDC unit

There were four equal channels of the TDC designed in high-reliability flash-FPGA (APA1000, from ACTEL Corp.) corresponding to the CFDs [16]. A couple of TDC channels were occupied by a valid event generating start and stop signals. As shown in Fig. 4, each channel TDC had a configurable 9-bit counter which constantly counted the clock signal, followed by a 9-bit register to record the counter value when the event signal arose. The 64 OR gates acted as delay units of a delay chain whose delay length surpassed the clock period of the TDC to interpolate the clock period and 64 DFFs used to record the arrival time of an event signal. After the value of the 64 DFFs was encoded into a 6-bit value by an encoder, both the coarse-time measurement stored in the 9-bit register and fine-time measurement after the 6-bit encoder in each TDC channel, representing the time of an event signal, were fed into a FIFO/RAM unit for data processing by subsequent units with the sequential management of the control unit. The TOF of an event, τ_{tof} , measured by a pair of TDC channels is expressed by Eq. (3):

$$\tau_{tof} = (N_{stop} - N_{start}) \times clk + \left(\frac{n_{start}}{m_{start}} - \frac{n_{stop}}{m_{stop}} \right) \times clk, \quad (3)$$

Fig. 4 (Color online) Block diagram of the TDC converter



where N_{start} and N_{stop} are the latched moments of the register for the start and stop signals, respectively; clk is the clock period; n_{start} and n_{stop} are the encoded fine moments for the start and stop signals, respectively; m_{start} and m_{stop} are the covered lengths for the start and stop channels in one clock and were measured by the code density test.

Furthermore, an event interval coincidence unit was added to determine and filter invalid events according to the time length threshold, which differed from the leading discriminator of the CFD whose function was to filter noise or interruptions.

2.3 Status monitoring unit

A precise monitor circuit (Fig. 5) was designed to collect the operating status of different aspects including all seven types of HV supply, multipoint temperature, and working currents. Twenty-two channels of status were asynchronously acquired via three multiplexes and shared a signal conditioning chain constituted by an amplifier, a 16-bit resolution ADC (AD976A), and 16-bit buffer protecting FPGA pins from overvoltage damage by providing an interface of shifting logic voltage from a + 5 V operation to + 3.3 V operation. Because both fixed HVs and the steps of sweeping HV (not the rising or descending interval of adjacent steps) changed slowly, the robust AD976A with 200 ksps sampling rate and > 83 dB S/N (the ratio of signal to noise) was adequate for accurate measurements of the various statuses. Another important feature was that the AD976A supported a ± 10 V range for analog input under a + 5 V supply environment, which is a significant benefit in enhancing the measuring precision under a large voltage difference, such as sweeping HV steps from several volts up to thousands of volts.

2.4 Control and data processing unit (CDPU)

The CDPU, whose function was to govern each unit and process both the science and status data, can be divided into nine parts, as shown in Fig. 6. Under different

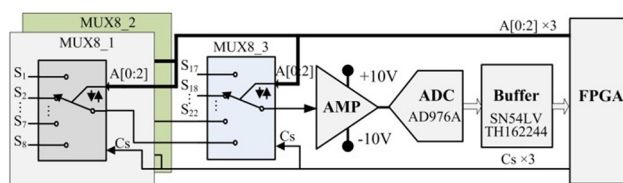


Fig. 5 (Color online) Simplified diagram of the status monitoring circuitry

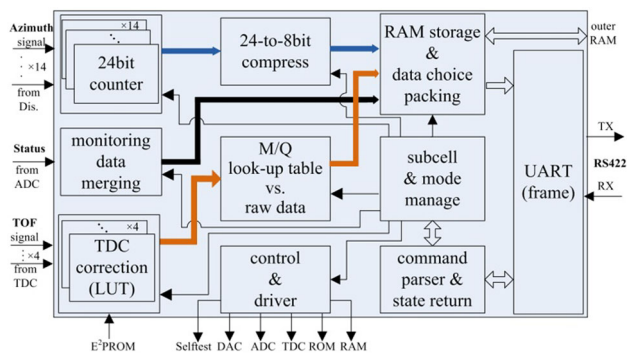


Fig. 6 (Color online) Block diagram of the CDPU

commands sent by a satellite computer and parsed by command parser unit, the subcell and mode manage unit was in charge of the other seven units. Incident events hitting different anodes at 32 energy steps were recorded by 14 counters (24-bit), followed by a 24-to-8-bit compressor before entering the RAM for cache. Details regarding the compression algorithm are given in Ref. [17]. The TDC data from the TOF signals was firstly online corrected by a correction algorithm based on INL compensation [18]. Then, the corrected TDC data were fed into a unit where either the raw data or data of mass-per-charge look-up table (M/Q LUT) was determined and sent to the RAM according to the TOF mode configuration. The M/Q LUTs were generated by a classification algorithm based on the basic relationships presented by Eq. (1) for various main species. The monitoring data from various statuses in an energy step emerged and were assembled, then written into the assigned areas in RAM. Under different working modes, various data which were optional from the TOF data, position data, and status parameters, were sent to the upper computer after data packing and framing. Owing to the confined capacity of the RAM in FPGA, an external RAM was exploited to increase storage space.

2.5 Other units

The control and regulation of different HV supplies for the spectrometer were accomplished by DAC circuits on readout electronics. A 16-bit DAC was used to exactly control the sweeping HV for the electrostatic analyzer,

while fixed HVs were set up by configuring 12-bit DACs (TLV5618) on the basis of potential demands. In order to obtain a 22.5° angular resolution of an incident particle, 14 channels of CEM signals were conditioned by A121 hybrid chips composed of amplification and discrimination circuitry that can cover 12 MHz event rates with a low noise level [19]. As for the HV supply of the detector, a similar design scheme is described in Ref. [17].

Additionally, 16 narrow pulse signals were furnished by a built-in test circuit to stimulate the CFDs and A121 s. The A121 s were allotted with 12 test signals, configured from 12 selectable repetitive frequencies with the largest periodic event rates up to 1 MHz to check each signal chain. While the other four test signals were allocated into two pairs of signals, and each pair had two optional fixed intervals at repetitive frequencies equal to that of the A121 s to check the CFD signal chain.

Because of the harsh radiation effects in the space environment, in particular single events effect (SEE) and total ionizing dose (TID) which are prone to cause damage or destruction to components [20], different techniques have been considered and adopted on our electronics to mitigate or eliminate these effects, for example, top priority to high-tolerance chips, triple module redundancy techniques, hardware redundancy, and watchdog technique for program exception. More details on radiation mitigation can be found in Refs. [17, 20].

3 Results

The timing accuracy of the CFD circuit and time resolution of the TDC circuit are the most important parameters for the TOF readout electronics [21]. An electronics test system was established for the performance test (Fig. 7a), and the electronics test is shown schematically in Fig. 7b, c. An ion beam based on a TOF system was also built to simulate ion species in the space environment to verify the time measurement performance.

3.1 Electronics test

3.1.1 CFD test

As shown in Fig. 7b, a signal generator (TEK AFG3252) output a channel of sharp negative pulse with 2 MHz repetitive frequency and a synchronizing signal (TTL level) that was immediately transmitted to an oscilloscope. The analog signal was firstly attenuated by a passive attenuator and then fed to one channel of the CFD whose attenuation ratio (f) was 0.3 and delay length (t_d) was set to 2 ns, generating a timing signal that was sent to another channel of the oscilloscope. By adjusting the

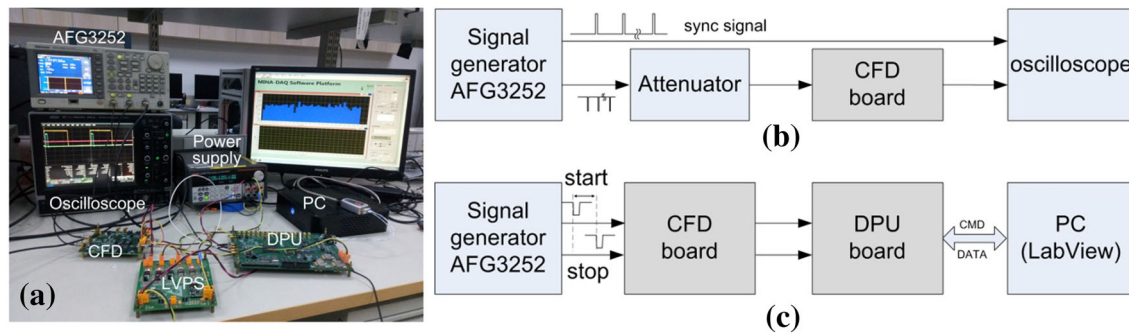


Fig. 7 (Color online) **a** Setup of electronics test, **b** the schematics of CFD test, **c** schematics of the TDC test

amplitude and leading edge of the negative pulse in a large range, simulating different detector signals, the timing error caused by the variation of the signal shape was measured on the basis of skew-time, which is the interval difference between the synchronizing (reference signal) and CFD timing signals. This error was the deviation of the skew-times viewed and counted on the oscilloscope. Considering an extra small deviation to the signal shape deviation by the smoothing of the passive attenuator, three leading edges (2.5, 3.5, and 4.5 ns) signals simulating the bad cases in the practical experiment were installed for the CFD timing testing. The relationship between the timing error and signal shape variation is shown in Fig. 8. Each curve showed a drastic drop in the amplitude range of 10–35 mV, becoming flat or changing little beyond 35 and up to 500 mV.

3.1.2 TDC test

A code density test was carried out to determine the nonlinearity of the TDC and then was combined with the fixed delay test (similar to the cable delay test) to ascertain

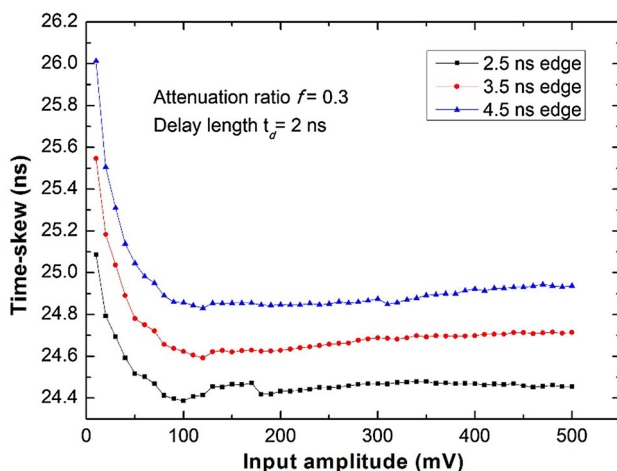


Fig. 8 (Color online) Relationship between the timing error and signal shape variation

the uncertainty of the TDC with statistical methods based on a large number of measurements of random input time intervals [18, 22], as shown in Fig. 7c. Two channels of negative random pulses produced by a generator with a repetitive frequency, sufficiently different from the reference clock of the TDC circuitry, and start and stop signals delayed by a fixed time relatively to the start signal, were fed into two channels of the CFD board. Then, a pair of timing signals generated by CFD was sent to the DPU board for the TDC measurement, and the data were transferred to an upper computer for the statistical analysis and displayed using a LabView program. As the timing signals were random to the TDC's clock signal, every delay unit of the delay chains in the TDC circuit was distributed with an amount of hits. The hits of each bin for one channel TDC were counted in the histogram shown in Fig. 9a. The code density test showed that the clock period (25 ns) of the TDC was interpolated into 46 parts by a delay chain, namely, a time resolution of ~ 550 ps was reached for the TDC. According to the difference between the counting of each bin and their ideal hitting number, both differential nonlinearity (DNL) and INL, normalized to the least significant bit (LSB), were obtained and shown in Fig. 9b. The fixed delay interval was also measured by subtracting the TDC values of the stop channel from those of the start channel. With a 635-ns delay interval installed on the generator, the time interval was recorded by the TDC and was shown without and with INL correction in Fig. 10a, b, respectively. The results with another $3.1 \mu\text{s}$ fixed delay are shown in Fig. 10c, d. Gaussian fitting was performed for the statistical results of both before and after INL correction. According to the statistical analysis, the time uncertainty expressed as the root mean square (RMS) was significantly reduced after the correction.

3.2 Beam test

A beam test system underground-based vacuum facility was constructed at the Hefei National Laboratory for Physical Sciences at Microscale. This TOF mass imaging

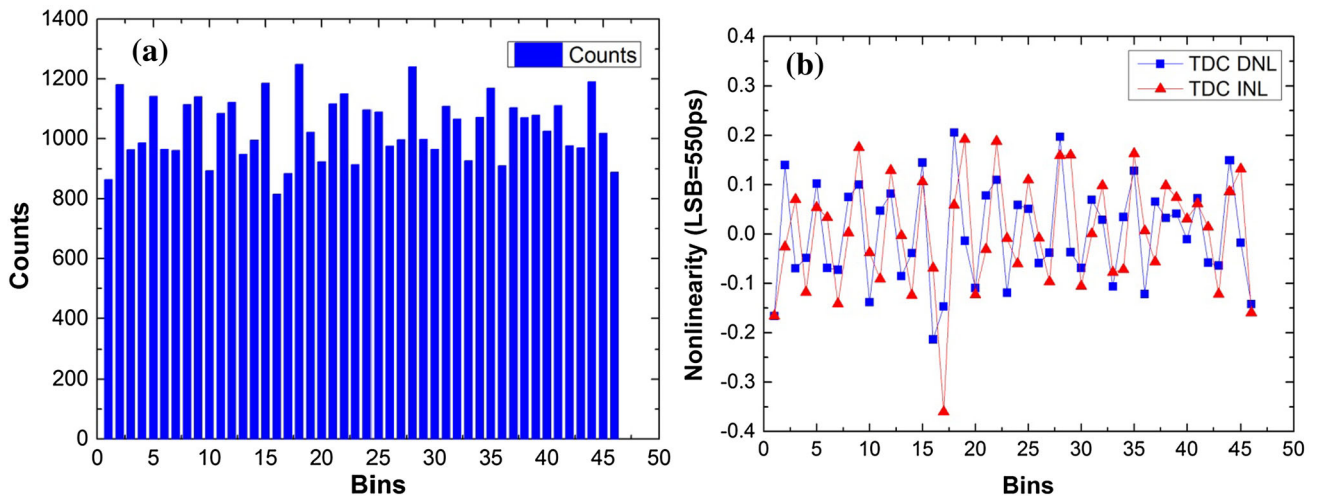


Fig. 9 (Color online) Result of the TDC nonlinearity test: **a** code density test, **b** DNL and INL tests

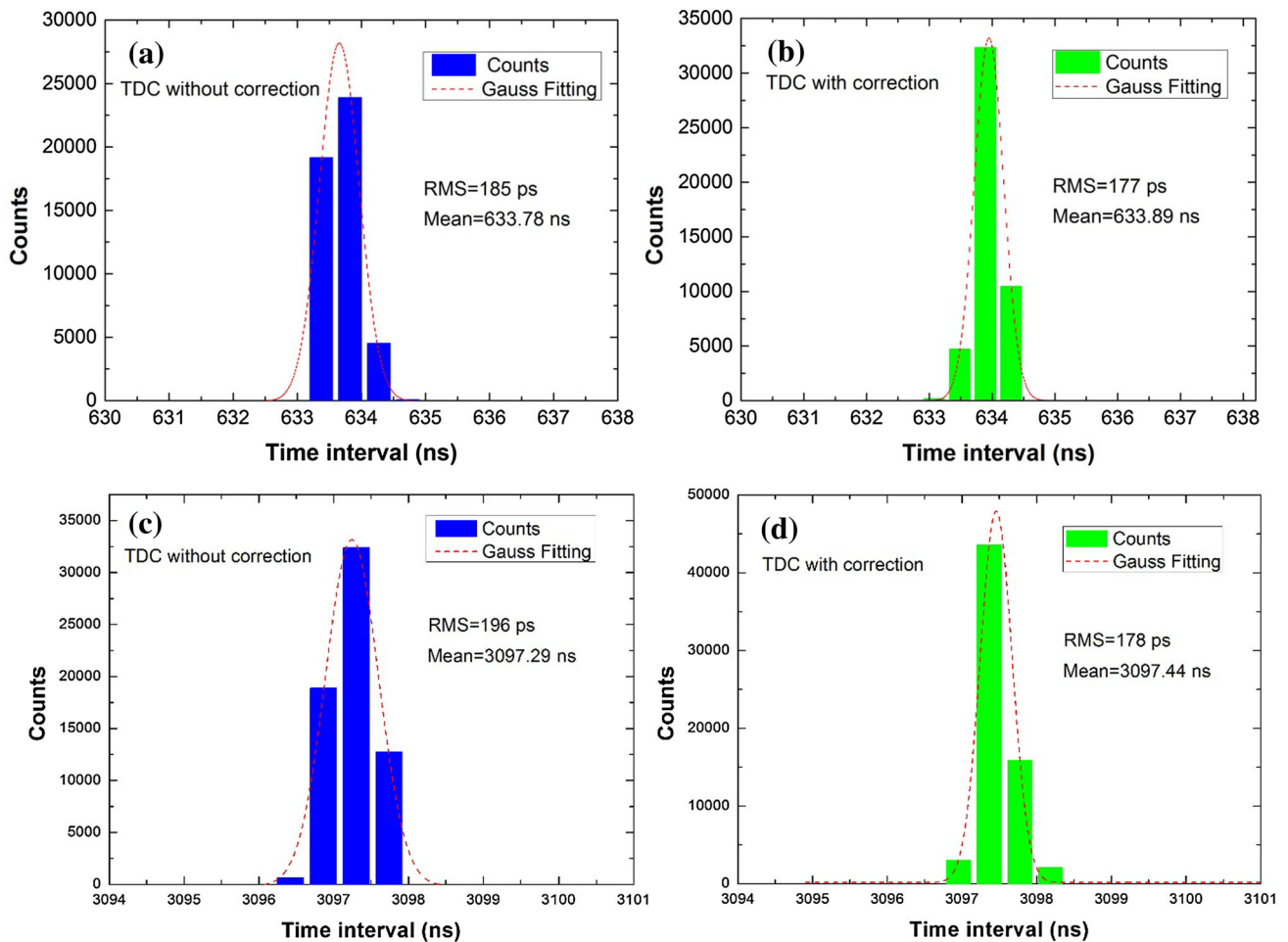


Fig. 10 (Color online) TDC uncertainty test under: **a** 635 ns fixed delay without INL correction, **b** 635 ns fixed delay with INL correction, **c** 3.1 μs fixed delay without INL correction, **d** 3.1 μs fixed delay with INL correction

system includes an electron gun chamber, a reaction chamber, and gas source, and a simplified schematic

diagram is shown in Fig. 11a. A pulsed electron beam from a thermal cathode electron gun is injected into the reaction

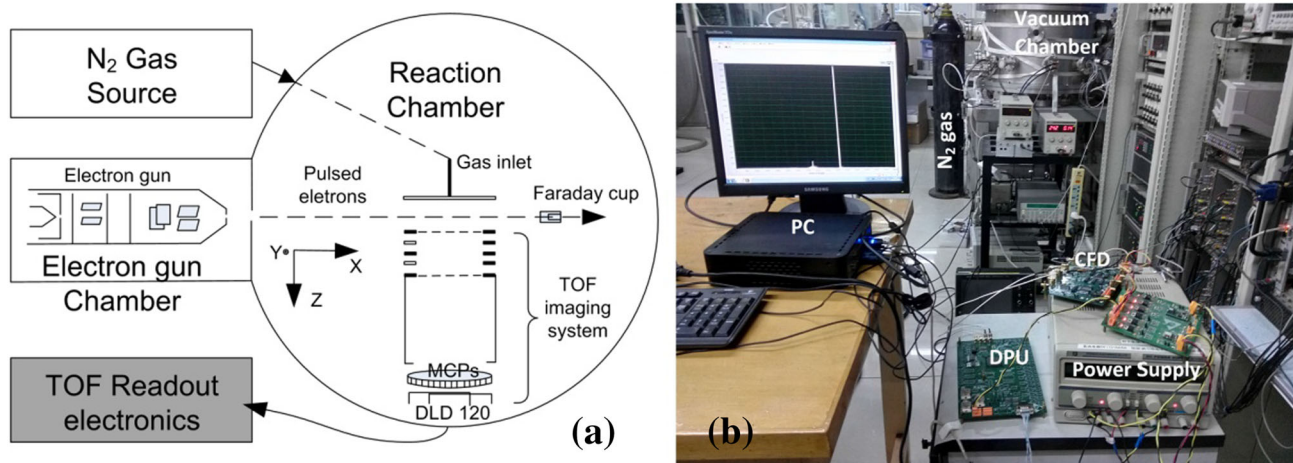


Fig. 11 (Color online) **a** Diagram of the beam test system. The TOF imaging was in the vacuum chamber, while the readout electronics was outside, **b** test field of the electron beam impacting on N_2 gas

chamber to collide with the gas target (N_2) at the reaction center. After collisions between the electrons and N_2 gas, a voltage pulse is applied on the pushing electrode to create a uniform field at the reaction area, aimed at extracting the fragment ions into the detection system composed of a pair of MCPs in chevron configuration followed by delay line anodes (DLD120). A more detailed description of the system is provided in Ref. [23].

The test field is shown in Fig. 11b. Our readout electronics were equipped with the TOF system using custom connectors and coaxial cables to receive a pair of TOF signals and measure the travel time of different species produced by collisions with a 362-eV electron beam. The TOF data were online processed and updated in real time when new packets were transmitted from the DPU board to the computer. Figure 12a shows the TOF spectrum of ions from the N_2 gas decomposition under a lot of statistical

data. The top most peak represented the species of N^{2+} , and the short peak with a broadening bottom was the pileup of both N^+ and N_2^{2+} ions. In addition, an existing experimental TOF readout system with time resolution < 50 ps from Hefei National Laboratory for physical sciences at microscale [23] was also applied to measure the TOF spectrum of the N_2 ion fragments, for comparison. The results are shown in Fig. 12b.

4 Discussion

4.1 CFD timing error

The test results confirmed that the CFD circuit reached a low timing dispersion of < 200 ps in the large amplitude range from ~ 35 to 500 mV (even more than 500 mV) for

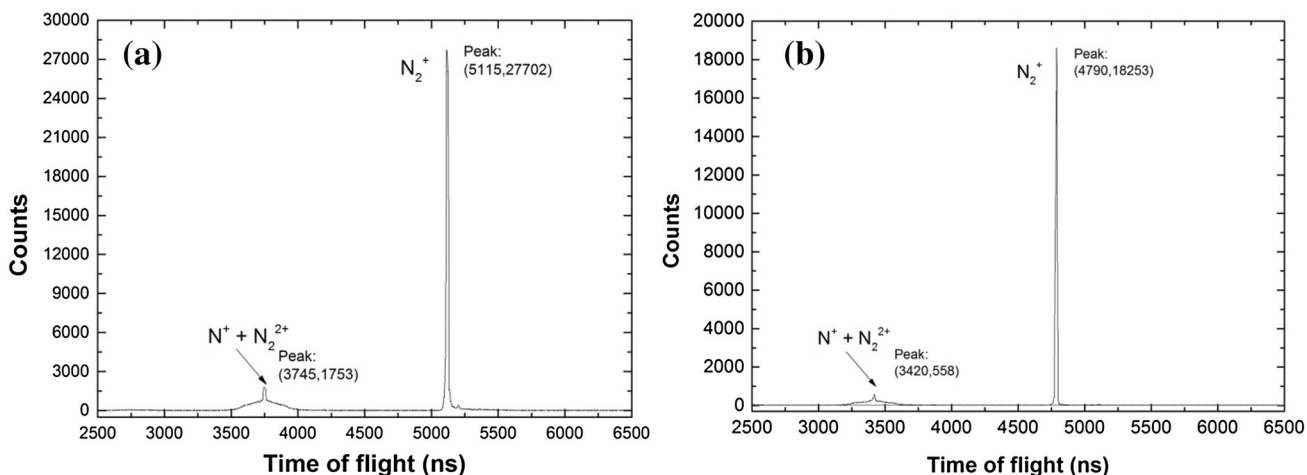


Fig. 12 TOF spectrum of ions produced from the 362-eV electron impact on the N_2 gas: **a** results of the TOF electronics, **b** test results of an existing experimental TOF readout system from the Hefei National Laboratory for Physical Sciences at Microscale

all three leading edges. Compared with the timing accuracy of < 300 ps for the ULEIS instrument on the ACE spacecraft [24], our CFD was capable of accomplishing precise timing for both MCPs and CEM detectors whose high gain and fluctuation effects yielded a broad pulse height distribution of typically tens to several hundred mV as reported by G Gloeckler [25]. In addition, a 2 MHz repetitive pulse was used due to the limit of the reference signal, but the CFD circuits can work normally beyond a 10 MHz input frequency, which significantly exceeds the requirement of the event rate for the physical experiment.

4.2 TDC range, resolution, and accuracy

As the coarse counter was configured as 8-bit, it can reach a dynamic range of $6.4 \mu\text{s}$ at 25 ns clock period. Owing to the non-uniformities in both the delay cells and routes in the FPGA, the TDC presents an INL of 0.36 (LSB) that led to an increase in measuring error for the fixed delay test. From the fixed delay test of 635 ns and $3.1 \mu\text{s}$, a better uncertainty of < 180 ps was clearly obtained with the INL correction. Compared with similar experiments, our TDC time resolution of ~ 550 ps was better than the 2.5 ns time resolution of the HOPE instrument which uses a similar technique (Van Allen probes mission) [13] and was also better than the time resolution (750 ps) of the ion mass spectrometer on the operating CASSINI mission [26]. These results indicate that our FPGA-TDC satisfies the time measurement demands.

4.3 TOF spectrum

In the electron beam test, the fragment ions from the N_2 decomposition were clearly discriminated by our readout electronics. Since the ionization cross sections for the production of N_2^+ were higher than those of the production of $\text{N}_2^{2+} + \text{N}^+$, the counts of N_2^+ in the TOF spectrum were much greater than those of $\text{N}^+ + \text{N}_2^{2+}$. This result is in line with H. C. Straub's measurement [27]. Moreover, by comparison, our TOF spectrum was similar to the results of the experimental TOF readout system, except for a fixed offset of ~ 330 ns, which was set to avoid the transient electromagnetic interference at the moment providing a strong extraction field for the start TDC channel in the experimental TOF readout system. Although the beam test was equipped with a TOF imaging system, this result suggests that our electronics works well for ion species measurements. A subsequent beam test for our TOF system with an ion composition analyzer is still currently being designed because of its complexity and elaboration.

5 Summary

A readout electronics has been successfully developed for a prototype TOF ion composition analyzer to measure M/Q for space plasmas, covering an energy range of 200–100 keV/e. A high event rate and low timing error were demonstrated for a large input range of ~ 35 –500 mV, as well as a ~ 550 ps time resolution with low uncertainty (< 180 ps) and $6.4 \mu\text{s}$ time range for the TOF measurement. In addition, the TOF spectrum measurement for ionic fragments of N_2 in the beam test demonstrated that our readout electronics exhibits a good performance and satisfies the physical requirements of the ion composition spectrometer.

Acknowledgements The authors are grateful for the help and discussion of collaboration teams from Hefei National Laboratory for Physical Sciences at Microscale and CAS Key Laboratory of Geospace Environment (USTC).

References

1. D.T. Young, B.L. Barraclough, D.J. McComas et al., CRRES low-energy magnetospheric ion composition sensor. *J. Spacecr. Rockets* **29**, 596–598 (1992). <https://doi.org/10.2514/3.25505>
2. R. Lundin, S. Barabash, H. Andersson et al., Solar wind-induced atmospheric erosion at Mars: first results from ASPERA-3 on Mars Express. *Science* **305**(5692), 1933–1936 (2004). <https://doi.org/10.1126/science.1101860>
3. S.M. Curry, J.G. Luhmann, Y.J. Ma et al., Response of Mars O⁺ pickup ions to the 8 March 2015 ICME: inferences from MAVEN data-based models. *Geophys. Res. Lett.* **42**, 9095–9102 (2015). <https://doi.org/10.1002/2015GL065304>
4. D.M. Klumpar, E. Möbius, L. M. Kistler et al, in *The FAST Mission*, ed. by R.F. Pfaff Jr. (Springer, Amsterdam, 2001), pp. 197–219
5. A.B. Galvin, L.M. Kistler, M.A. Popecki et al., The plasma and suprathermal ion composition (PLASTIC) investigation on the STEREO observatories. *Space Sci. Rev.* **136**, 437–486 (2008). <https://doi.org/10.1007/s11214-007-9296-x>
6. J.P. McFadden, O. Kortmann, D. Curtis et al., MAVEN suprathermal and thermal ion composition (STATIC) instrument. *Space Sci. Rev.* **195**(1), 199–256 (2015). <https://doi.org/10.1007/s11214-015-0175-6>
7. J.S. Halekas, E.R. Taylor, G. Dalton et al., The solar wind ion analyzer for MAVEN. *Space Sci. Rev.* **195**, 125–151 (2015). <https://doi.org/10.1007/s11214-013-0029-z>
8. J.E. Nordholt, J.J. Berthelier, D.M. Burr et al., Measurement Techniques, in *Space Plasmas: Particles*, ed. by R.F. Pfaff, J.E. Borovsky, D.T. Young (American Geophysical Union, Washington, DC, 1998), pp. 209–214
9. E. Möbius, L.M. Kistler, M.A. Popecki et al., Measurement Techniques, in *Space Plasmas: Particles*, ed. by R.F. Pfaff, J.E. Borovsky, D.T. Young (American Geophysical Union, Washington, DC, 1998), pp. 243–248
10. F.M. Yang, P.C. Huang, W.Z. Chen et al., Progress on laser time transfer project, in *Paper Presented at 15th International Workshop on Laser Ranging* (Canberra, 15–20 October 2006)
11. W. Hsiang, S. Huntzicker, K. King et al., Performance and area tradeoffs in space-qualified FPGA-based time-of-flight systems,

- in *Paper Presented at the 9th International Conference on Electronic Measurement and Instruments* (Beihang University, Beijing, 16–19 August 2009)
12. X. Qin, C.Q. Feng, D.L. Zhang et al., Development of a high resolution TDC for implementation in flash-based and anti-fuse FPGAs for aerospace application. *IEEE Trans. Nucl. Sci.* **60**, 3550–3556 (2013). <https://doi.org/10.1109/TNS.2013.2280919>
 13. H.O. Funsten, R.M. Skoug, A.A. Guthrie et al., Helium, oxygen, proton, and electron (HOPE) mass spectrometer for the radiation belt storm probes mission. *Space Sci. Rev.* **179**, 423–484 (2013). <https://doi.org/10.1007/s11214-013-9968-7>
 14. Q. Shen, *The research on high resolution time to digital conversion for quantum communication* (Ph.D. Thesis, University of Science and Technology of China, 2013)
 15. N. Paschalidis, N. Stamatopoulos, K. Karadamoglou et al., A time-of-flight system on a chip suitable for space instrumentation, in *Paper Presented at the 2001 IEEE Nuclear Science Symposium Conference Record* (San Diego, 4–10 November 2001)
 16. J.J. Wang, Radiation effects in FPGAs, in *Paper Presented at the Proceedings of the 9th Workshop on Electronics for LHC Experiments* (Amsterdam, 29 Sept–3 Oct 2003)
 17. D. Yang, Z. Cao, X. Qin et al., Readout electronics of a prototype spectrometer for measuring low-energy ions in solar wind plasma. *Nucl. Sci. Technol.* **27**, 135 (2016). <https://doi.org/10.1007/s41365-016-0136-0>
 18. S.B. Liu, C.Q. Feng, H. Yan et al., LUT-based non-linearity compensation for BES III TOF's time measurement. *Nucl. Sci. Technol.* **21**, 49–53 (2010). <https://doi.org/10.13538/j.1001-8042/nst.21.49-53>
 19. A121 hybrid charge sensitive preamplifier, discriminator, and pulse shaper (Amptek Inc., USA). <http://amptek.com/products/a121>. Accessed 12 Sept 2015
 20. R.H. Maurer, M.E. Fraeman, M.N. Martin et al., Harsh environments: space radiation environment, effects, and mitigation. *J. Hopkins APL Tech. D* **28**, 17 (2008)
 21. X. Qin, C.Q. Feng, D.L. Zhang et al., A low dead time vernier delay line TDC implemented in an actel flash-based FPGA. *Nucl. Sci. Technol.* **24**, 040403 (2013). <https://doi.org/10.13538/j.1001-8042/nst.2013.04.012>
 22. R. Pelka, J. Kalisz, R. Szplet, Nonlinearity correction of the integrated time-to-digital converter with direct coding. *IEEE Trans. Instrum. Meas.* **46**, 449–453 (1997). <https://doi.org/10.1109/19.571882>
 23. E.L. Wang, X. Shan, Y.F. Shi et al., Momentum imaging spectrometer for molecular fragmentation dynamics induced by pulsed electron beam. *Rev. Sci. Instrum.* **84**, 123110 (2013). <https://doi.org/10.1063/1.4847156>
 24. G.M. Mason, R.E. Gold, S.M. Krimigis et al., The ultra-low-energy isotope spectrometer (ULEIS) for the ACE spacecraft. *Space Sci. Rev.* **86**, 409–448 (1998). <https://doi.org/10.1023/A:1005079930780>
 25. G. Gloeckler, K.C. Hsieh, Time-of-flight technique for particle identification at energies from 2–400 keV/nucleon. *Nucl. Instrum Methods* **165**, 537–544 (1979). [https://doi.org/10.1016/0029-554x\(79\)90636-0](https://doi.org/10.1016/0029-554x(79)90636-0)
 26. D.T. Young, J.J. Berthelier, M. Blanc et al., Cassini plasma spectrometer investigation. *Space Sci. Rev.* **114**, 1–112 (2004). <https://doi.org/10.1007/s11214-004-1406-4>
 27. H.C. Straub, P. Renault, B.G. Lindsay et al., Absolute partial cross sections for electron-impact ionization of H₂, N₂, and O₂ from threshold to 1000 eV. *Phys. Rev. A* **54**, 2146 (1996). <https://doi.org/10.1103/PhysRevA.54.2146>